

# Ultrabroadband Light Coupling for Integrated Photonics via Nonadiabatic Pumping

Weiwei Liu, Chijun Li, Bing Wang,\* Tianyan Chai, Lingzhi Zheng, Zhuoxiong Liu, Xiaohong Li, Cheng Zeng,\* Jinsong Xia, and Peixiang Lu\*

Enlarging bandwidth capacity of the integrated photonic systems demands efficient and broadband light coupling among optical elements, which is a vital issue in integrated photonics. Here, an ultrabroadband light coupling strategy based on nonadiabatic pumping is developed, and the designs in thin-film lithium niobate on insulator platform are experimentally demonstrated. It is found that nonadiabatic transition produces a decreased dispersion of the phases related to eigenstates in the waveguides. As a consequence, high-efficiency and dispersionless directional transfer are realized between edge states, which leads to an ultrabroadband light coupling covering a 1 dB bandwidth of  $\approx 320$  nm in experiment ( $>400$  nm in simulation), with a length ( $\approx 50$   $\mu\text{m}$ )  $\approx 1/10$  of that required in conventional adiabatic transfer approach. Moreover, the coupling strategy exhibits a low insertion loss ( $<1$  dB), a low crosstalk ( $<-10$  dB), and a great robustness against structural deviations ( $\approx 100$  nm). Furthermore, complex functional devices including beamsplitter and multiple-level cascaded networks are constructed for broadband light routing and splitting. This work preserves significant advantages simultaneously in extending the operation bandwidth to all of the optical communication bands and minimizing the footprint, which demonstrates great potential for large-scale photonic integration and high-speed information processing on chip.

the massive data transfer and high-bandwidth-density interconnects, on-chip parallel wavelength division multiplexing (WDM) has been considered as an important technology to largely enhance the data capacity.<sup>[8]</sup> To realize WDM in compact photonic integrated circuits, broadband light coupling among waveguides plays an important role in light transmission and optical interconnection. However, due to serious material and waveguide dispersion, light coupling is highly sensitive to structure and wavelength. As a consequence, the response bandwidth and data capacity will be severely restricted by the existing bottlenecks. The urgent need to enlarge bandwidth capacity of the integrated photonic systems demands efficient and broadband light coupling among optical elements. Currently, a variety of effective approaches have been proposed and demonstrated for achieving the desired light coupling, including adiabatic transfer,<sup>[9,10]</sup> phase matching,<sup>[11]</sup> dispersion control,<sup>[12]</sup> and topological protection.<sup>[13]</sup> One notable

## 1. Introduction

The rapid advancement of integrated photonics has opened the way for massive and high-speed data transfer on chip. These unique advantages lead to extensive applications including optical communications,<sup>[1,2]</sup> optical computing,<sup>[3–5]</sup> quantum information processing,<sup>[6,7]</sup> and so on. In order to deal with

example is the stimulated Raman adiabatic passage,<sup>[9,14]</sup> which allows selective population transfer between coupling waveguides via an intermediate state, and is insensitive to the coupling strength in the adiabatic limit. However, it requires a long coupling configuration to ensure efficient adiabatic transfer, thus resulting in highly elongated waveguides and decreased integration density.<sup>[10]</sup> More recently, artificial gauge field is developed to engineer the coupling dispersion among waveguides,<sup>[15]</sup> which are beneficial for realizing broadband dispersionless coupling to certain extents. Nevertheless, most designs can hardly satisfy the demand of covering the full optical communication bands for on-chip WDM (1270–1625 nm). Therefore, the realization of high-performance light coupling with ultrabroad bandwidth, high coupling efficiency, and small interaction length still remains challenging.

As one of the most intriguing effects in quantum mechanics, topological pumping describes quantized transport of charge through an adiabatic cyclic evolution of the underlying Hamiltonian.<sup>[16]</sup> Because of the worthwhile topological features, it has garnered significant attention from diverse platforms such as semiconductor quantum dots,<sup>[17]</sup> cold atoms,<sup>[18,19]</sup>

W. Liu, C. Li, B. Wang, T. Chai, L. Zheng, Z. Liu, C. Zeng, J. Xia, P. Lu  
Wuhan National Laboratory for Optoelectronics and School of Physics  
Huazhong University of Science and Technology  
Wuhan, Hubei 430074, China  
E-mail: wangbing@hust.edu.cn; zengchengwuli@hust.edu.cn;  
lupeixiang@hust.edu.cn

X. Li, P. Lu  
Hubei Key Laboratory of Optical Information and Pattern Recognition  
Wuhan Institute of Technology  
Wuhan, Hubei 430205, China

 The ORCID identification number(s) for the author(s) of this article can be found under <https://doi.org/10.1002/lpr.202401492>

DOI: 10.1002/lpr.202401492

quasicrystals,<sup>[20,21]</sup> acoustics,<sup>[22]</sup> quantum gas,<sup>[23]</sup> and synthetic-dimension systems.<sup>[24,25]</sup> In particular, coupled optical waveguides have offered an ideal photonic platforms for exploring topological pumping by constructing a cycle in the parameter space.<sup>[26–29]</sup> Adiabatic transport of edge states in waveguide arrays has been demonstrated utilizing this interesting mechanism, and it provides a favorable approach for realizing broadband light coupling with robustness which is immune to structural perturbations and fabrication disorders.<sup>[30]</sup> Moreover, it has been demonstrated that the topologically protected transfer can still happen with half-cycle topological pumping in finite lattices,<sup>[31]</sup> and fast Thouless pumps were realized by non-Hermitian Floquet engineering in which nonadiabatic transitions were suppressed with time-periodic dissipation.<sup>[32]</sup> Nevertheless, edge state transfers based on adiabatic evolution and Floquet-driven system both request a large interaction length, which imposes a trade-off between the response bandwidth and small footprint. The nonadiabatic effects,<sup>[22,33,34]</sup> exhibiting tremendous distinctions in the interaction mechanism and showing great potential for resolving the contradictions, require further exploration.

In this work, a compact and ultrabroadband light coupling strategy is developed based on nonadiabatic pumping in optical waveguide arrays, and the designs are further experimentally demonstrated in thin-film lithium niobate on insulator (LNOI) platform. Nonadiabatic pumping is created in finite off-diagonal Aubre–Andre–Harper (AAH)-modeled photonic waveguides away from the adiabatic limitation. In this regime, a high-efficiency directional transfer of the incident light to the other edge can happen, which enables to achieve an ultrabroadband light coupling covering a 1 dB bandwidth of  $\approx 320$  nm in experiment ( $>400$  nm in simulation), with a coupling length  $\approx 1/10$  of that required for adiabatic transfer. Moreover, the nonadiabatic-pumping-based light coupling exhibits a high performance with a low insertion loss ( $<1$  dB), a low crosstalk ( $<-10$  dB), and a great robustness against structural deviations ( $\approx 100$  nm). Furthermore, broadband beamsplitter and multiple-level cascaded networks are constructed for light routings. This result preserves significant advantages simultaneously in extending the operation bandwidth and minimizing the footprint, which demonstrates great potential for large-scale photonic integration and high-speed information processing on chip.

## 2. Theoretical Model

We start by considering the 1D off-diagonal AAH model, which can be also connected with the topological pumping of a Su–Schrieffer–Heeger (SSH) chain with  $N$  of sites ( $N$  is odd, **Figure 1a**).<sup>[35]</sup> The system composes of a series of single mode waveguides that represent sites of a tight binding lattice. Topological pumping can be realized by varying the coupling strengths  $J_1$  and  $J_2$  between neighboring lattice sites. Light propagation in the waveguide array can be described by the tight-binding Hamiltonian

$$H = t \sum_{n=1}^N c_n^\dagger c_n + \sum_{n=1}^N [J_0 + (-1)^n \Delta J(z)] c_n^\dagger c_{n+1} + h.c. \quad (1)$$

Here,  $c_n^\dagger$  and  $c_n$  are the creator and annihilator on lattice site  $n$ , respectively.  $t$  represents the on-site potential, which is a constant

for the off-diagonal AAH model. The second term in Equation (1) represents the couplings between the nearest-neighbor waveguides with a constant (staggered) coupling strength  $J_0$  [ $\Delta J(z)$ ], which could be manipulated by adjusting the waveguide separations. The distance between neighboring waveguides are defined as  $d = d_0 + \Delta d \cos(2\pi z/P)$  [ $d = d_0 - \Delta d \cos(2\pi z/P)$ ], where  $z$  is the propagation distance and  $P = 2L$  is the modulation period. Correspondingly, the coupling strengths can be approximately expressed as  $J_1 = J_0 - \Delta J \cos(2\pi z/P)$  [ $J_2 = J_0 + \Delta J \cos(2\pi z/P)$ ] (see Section S1 in the Supporting Information). Since the edge state transfer can happen with half-cycle pumping, the total length of the waveguide array is set to  $L$ , as illustrated in the bottom panel of **Figure 1a**. By diagonalizing the Hamiltonian in Equation (1), we get the energy spectrum of this system, as shown in **Figure 1b**. There is exactly a zero-energy eigenstate lying in the bandgap, which is an edge state with light localized at the left edge for  $z = 0$ , as clearly displayed in the top panel of **Figure 1b**. With the increases of propagation distances  $z$ , the bandgap reduces gradually and nearly closes at  $z = L/2$  ( $\Delta J = 0$ ). Correspondingly, the localized state would be diverged at this gap-closing point, and then fully transferred to the right edge of the waveguide array for  $z = L$ . Moreover, this feature of the state transfer is essentially independent on the number of the lattice sites (waveguides), as the edge state still remains for the least lattice of  $N = 3$ . One critical issue for the adiabatic pumping of the edge states lies on that the energy transfer should be fully adiabatic all over this process. The adiabatic condition can be expressed as<sup>[31]</sup>

$$\eta = \frac{\sqrt{\Delta J \Omega}}{\Delta E} \ll 1 \quad (2)$$

where  $\Delta J$  is the variation amplitude of the coupling strength, and  $\Omega$  is the spatial modulation frequency,  $\Omega = 2\pi/P$ .  $\Delta E$  represents the energy gap between the adjacent states. The adiabatic condition is quantitatively analyzed by adopting a waveguide array with  $N = 3$ , for instance. Thin-film LNOI is selected to construct the coupled waveguide structure, due to its wide transparency window and small material dispersion.<sup>[36]</sup> **Figure 1c** maps  $\eta$  as function of the waveguide length and wavelength. It indicates that an interaction length larger than  $\approx 200$   $\mu\text{m}$  is required to realize adiabatic transfer over a broad band ( $\eta = 0.3$ ), and a much longer length over  $\approx 500$   $\mu\text{m}$  is required to achieve a high transfer efficiency (see Section S1 in the Supporting Information), which is not beneficial for achieving compact light coupling on chip.

In order to obtain a broadband and efficient excitation transfer with compact waveguides, light propagation in the waveguides is investigated under a nonadiabatic regime. With the paraxial approximation, light transfer in coupled waveguides can be calculated by the following coupled mode equation

$$i \frac{\partial \Psi}{\partial z} = H \Psi \quad (3)$$

where  $H$  is the systematic Hamiltonian described by Equation (1) for  $N = 3$ .  $\Psi$  is the complex amplitude of the electric field in the waveguides. Assumed that an edge state of  $\Psi(0) = [1, 0, 0]^T$  is incident from input port of the waveguides. The incident field can be decomposed as  $\Psi(0) = a_1(0)\Psi_1(0) + a_2(0)\Psi_2(0) + a_3(0)\Psi_3(0)$ , where  $\Psi_n(0)$  ( $n = 1, 2, 3$ ) represent the eigenstates of the

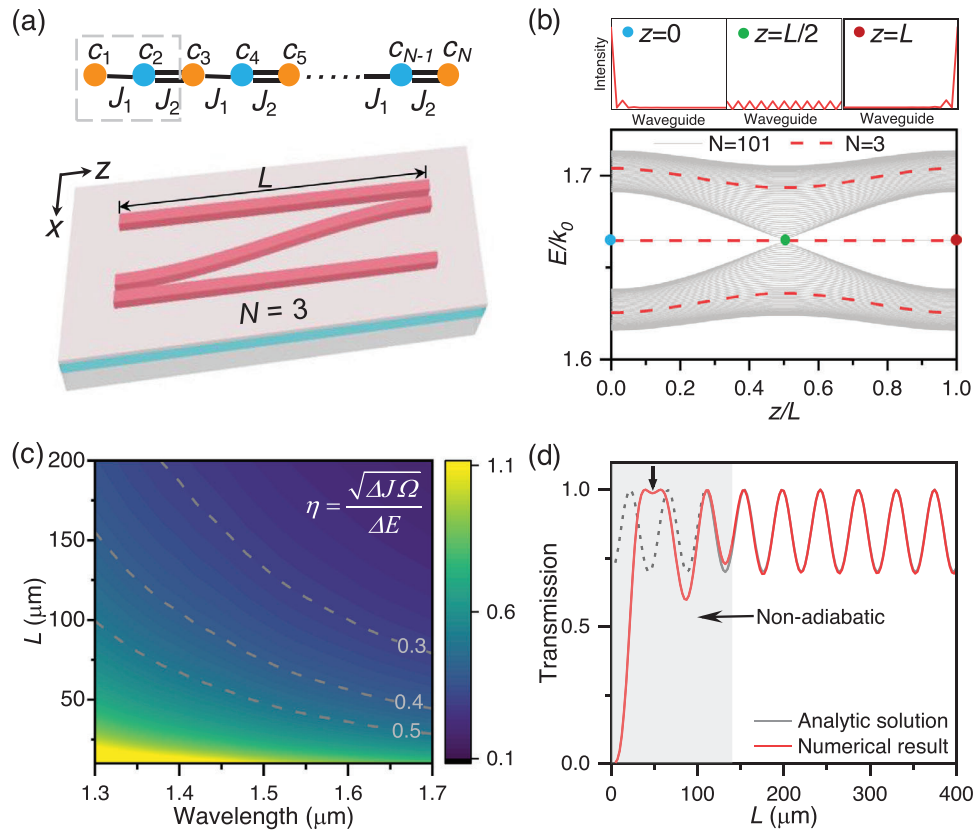


**Figure 1.** Topological pumping in optical waveguides. a) Schematic of a SSH chain with an odd number of sites and a waveguide array ( $N = 3$ ) for topological pumping of edge states. b) Energy spectra versus the normalized propagation length ( $z/L$ ) in a chain comprising  $N = 101$  and  $N = 3$  sites, respectively. Up panel shows eigenstates of the chain at  $z = 0$ ,  $L/2$ , and  $L$ . c) Mapping of the adiabatic condition factor as functions of wavelength and waveguide length. d) Normalized field intensities (transmission) at the output port as a function of the waveguide length, solved by numerical method and analytic solution, respectively.

coupled waveguides at  $z = 0$ . In the adiabatic process, transfer of the states happens with the corresponding weight coefficients of the eigenstates remaining unchanged ( $[a_1(0), a_2(0), a_3(0)]$ ). However, in the nonadiabatic regime, the eigenstates corresponding to different bands would transit to each other, resulting in propagation-dependent weight coefficients in the evolution,<sup>[35]</sup> i.e.,  $[a_1(z), a_2(z), a_3(z)]$ . Correspondingly, the field distribution in the waveguides can be expressed as

$$\Psi(z) = \left[ a_1(z)\Psi_1(z)e^{-i\Delta\varphi} + a_2(z)\Psi_2(z) + a_3(z)\Psi_3(z)e^{i\Delta\varphi} \right] e^{i\varphi} \quad (4)$$

where  $\varphi = \int \beta(z)dz$  representing the propagation phase of the zero-energy eigenstate.  $\Delta\varphi$  is the phase contrast between the adjacent modes, which originates from the mismatch of propagation constants and nonadiabatic transition (see Section S1 in the Supporting Information). The coupled mode equation Equation (3) is exactly solved by numerical method to explore the light transfer process. Figure 1d shows the normalized field intensity (transmission) in the corresponding edge waveguide of output port, monitoring as a function of the waveguide length  $L$ . In the adiabatic region, the transmission exhibits strong oscillation versus  $L$ , and the numerically solved results are consistent with the

analytic solution, which can be attributed to the phase mismatching and interference of the eigenstates (see Section S1 in the Supporting Information). By contrast, away from the adiabatic region, the transmission increases sharply first with the waveguide length, and we can still find a high transmission peak at around  $L = 50 \mu\text{m}$ , suggesting a high-efficiency transfer of the incident edge state.

### 3. Results and Discussions

#### 3.1. Numerical Simulations and Design

Since Equation (4) indicates that the accumulated phase contrast ( $\Delta\varphi$ ) plays an important role for the superposition of eigenstates in the coupled waveguides, it is analyzed to reveal the potential mechanism for transmission peak. Figure 2a presents a mapping of  $\Delta\varphi/\pi$  between adjacent eigenstates at the output port for the nonadiabatic pumping transition. The dispersion of  $\Delta\varphi$  increases with the waveguide length, and there exists a small dispersion even in the strong nonadiabatic region of  $L < 70 \mu\text{m}$ , implying that the nonadiabatic transition process is beneficial for producing a decreased dispersion of  $\Delta\varphi$ . Specifically, for a waveguide length around  $55 \mu\text{m}$ ,  $\Delta\varphi$  is close to zero for

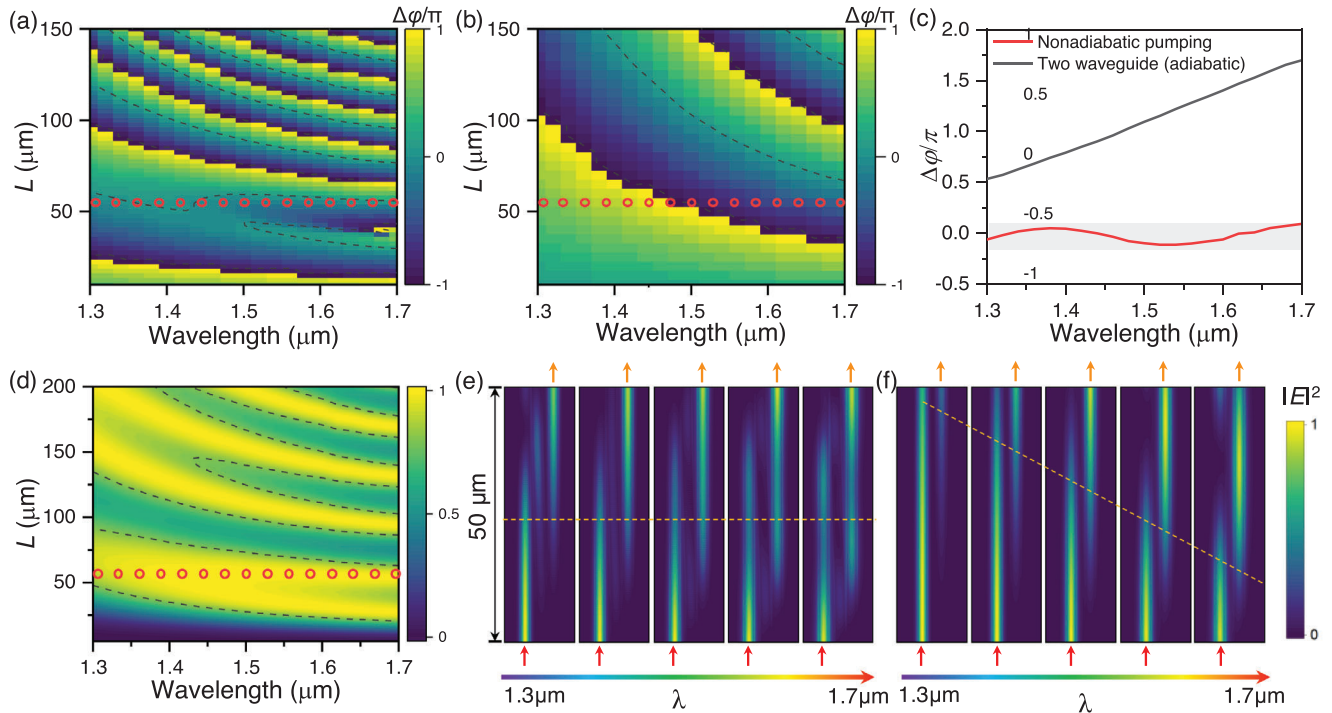


**Figure 2.** Nonadiabatic pumping and transfer of edge state. Mappings of the total accumulated phase contrast ( $\Delta\varphi/\pi$ ) between adjacent eigenstates at the output port, for a) the nonadiabatic pumping transition and b) that of the two-waveguide structure, respectively. The black dashed curves label an accumulated phase contrast of integer multiple of  $2\pi$ . c) Plots of the phase contrast  $\Delta\varphi$  as a function of wavelength at  $L = 55 \mu\text{m}$ , for the nonadiabatic pumping (red curve) and the two-waveguide structure (black curve), respectively. d) Mapping of transmission as functions of waveguide length and wavelength. The contour lines represent a transmission larger than 0.8 ( $-1 \text{ dB}$ ). Simulated field distributions ( $|E|^2$ ) in the LN waveguides of e) the nonadiabatic pumping design and f) conventional DC composed of two coupled waveguides, respectively.

all the calculated wavelength, as labeled by the black dashed curve and red circles. As a result, the three eigenstates can be constructively superposed at the output port of the waveguides, which explains the origin of the transmission peak at around  $L = 50 \mu\text{m}$  in Figure 1d. For comparison, the phase contrast between the even and odd eigenstates of a conventional directional coupler composed of two coupled waveguide is calculated, as shown in Figure 2b. In this structure, the accumulated phase contrast is proportional to the coupling strength between the two waveguide,  $\Delta\varphi = (\beta_{\text{even}} - \beta_{\text{odd}})L = 2J_0L$ ,<sup>[30]</sup> suggesting a serious dispersion of the two-waveguide structure. The phase contrasts  $\Delta\varphi$  for the two structures at  $L = 55 \mu\text{m}$  are extracted as a function of wavelength, as plotted in Figure 2c, which demonstrate an evidently decreased dispersion in the nonadiabatic pumping. Importantly, the decreased dispersion is advantageous for realizing a high-efficiency and broadband transfer of the edge state. To confirm this prediction, Figure 2d displays a continuous mapping of the transmission as functions of the waveguide length  $L$  and wavelength. It can be notably observed that the transmission is nearly unity and experiences little dispersion around  $L = 55 \mu\text{m}$ , all over the calculated wavelength range from 1.3 to 1.7  $\mu\text{m}$ . Therefore, it demonstrates an effective approach for achieving ultrabroadband light transfer of the edge state, with an interaction length less than 1/10 of that required in the adiabatic regime ( $>500 \mu\text{m}$ , see Section S1 in the Supporting Information).

To verify the theoretical results in practice, waveguide structures are designed and based on X-cut thin-film LNOI (300 nm LN layer). LN ridge waveguides are designed to have a top width of 650 nm, and the etch depth is 200 nm with a remaining slab of 100 nm, which allows for fundamental transverse electric like (TE) mode around 1550 nm. The separation between the top and middle waveguides is set as  $d = d_0 + \Delta d \cos(2\pi z/P)$ , with  $d_0 = 420 \text{ nm}$ ,  $\Delta d = 200 \text{ nm}$ . Silicon dioxide film is covered on the device for cladding. 3D full-wave simulations are performed using a commercial finite-difference time-domain analysis solver (see Section S2 in the Supporting Information). Fundamental TE mode of an individual waveguide is incident as the light source, which represents the initial edge state of  $\Psi(0) = [1, 0, 0]^T$ . Figure 2d presents simulated field distributions ( $|E|^2$ ) in the LN waveguides for the nonadiabatic pumping structure. The whole length of the interaction region ( $L$ ) is optimized to be  $\approx 50 \mu\text{m}$  for experiment. One can observe that the input state can be highly transferred to opposite edge at the output port, and simulated results are consistent with the theoretical prediction that light distribution in the intermediate waveguide suggests a nonadiabatic transfer process. More importantly, the high-efficiency transfer of edge state happens in a broadband spanning from 1.3 to 1.7  $\mu\text{m}$ , suggesting an operation bandwidth over 400 nm. By contrast, for conventional two-waveguide directional coupler (DC) with an identical interaction length, light coupling only exhibits a narrowband response from 1.5 to 1.6  $\mu\text{m}$ , as shown in Figure 2e.

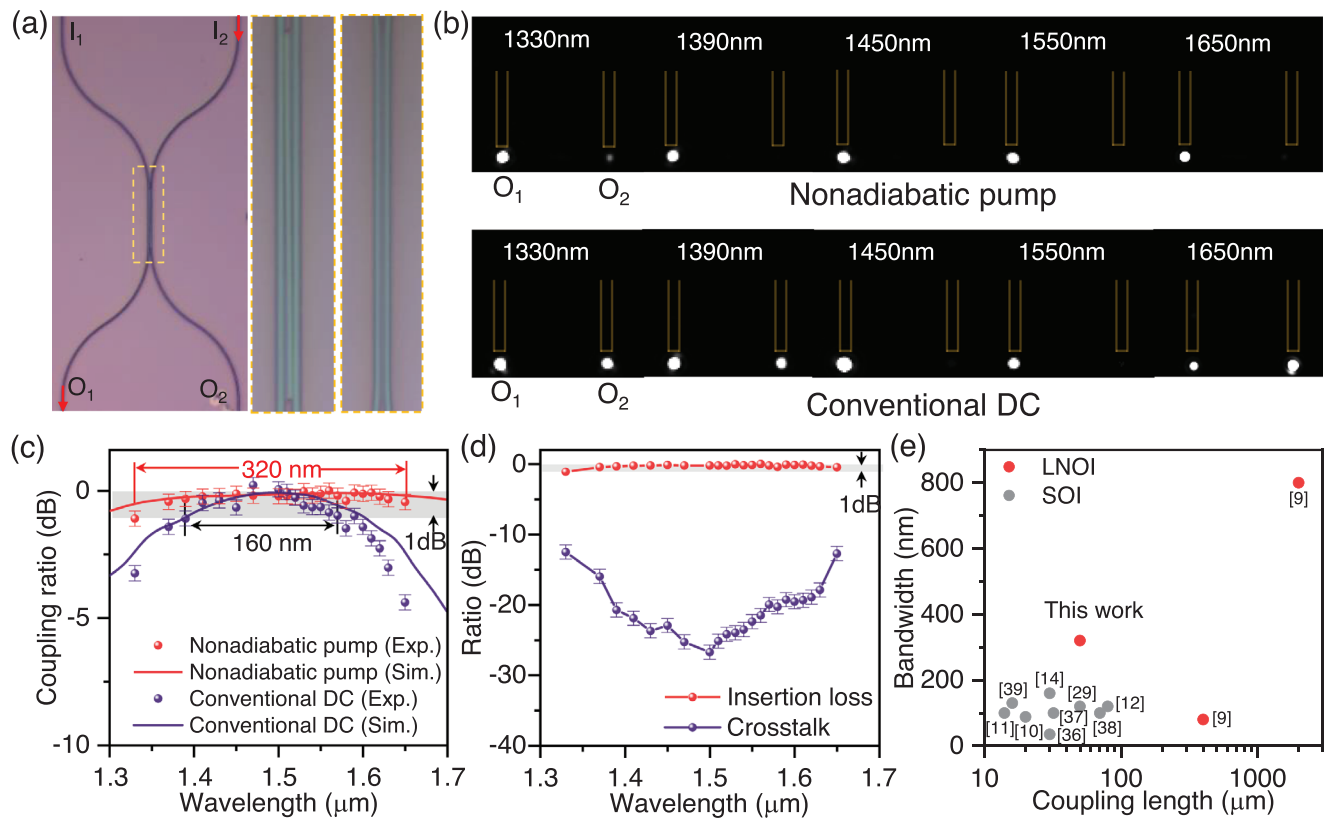


**Figure 3.** Experimental demonstration of ultrabroadband light coupling on chip. a) Microscopic image of the samples on a LNOI platform. b) Experimentally imaged scattering fields from output ports of the nonadiabatic pumping device and conventional DC, respectively, at different wavelengths (1330, 1390, 1450, 1550, and 1650 nm). c) Plots of measured and simulated coupling ratios for nonadiabatic pumping device and conventional DC, respectively. d) Plots of insertion loss and crosstalk of the nonadiabatic pumping device. e) Summary and comparison of the experimentally measured performances of typical broadband coupling designs on LNOI and SOI platforms.

### 3.2. Experimental Demonstration on LNOI Platform

In order to demonstrate the ultrabroadband light coupling strategy in experiment, LN waveguides were fabricated using standard nanofabrication process (see Section S2 in the Supporting Information). Near-infrared lasers covering the optical communication bands (1330–1650 nm) are used as light sources. The input and output ports are both tapered and polished, and lens fibers are used for efficiently coupling single-frequency laser with various wavelengths into (out of) the chip. A high-performance spectrometer (AQ6370B, Yokogawa) is used to measure the transmission spectra, and a near-infrared camera (991SWIR, Artray) is used to image the light spots from end facet of the waveguides under a microscope.

Figure 3a shows the microscopic image and the corresponding enlarged parts of the fabricated samples, with a conventional DC structure for comparison. Figure 3b shows experimentally measured output spots of the nonadiabatic pumping device and conventional DC, respectively, at wavelengths of 1330, 1390, 1450, 1550, and 1650 nm. As observed, for the nonadiabatic device, the input signal ( $I_2$ ) can be almost transferred to the crossing output port ( $O_1$ ), with nearly none optical signal outgoing from the other port ( $O_2$ ). For comparison, the coupling property of the conventional DC varies strongly at different wavelengths. Figure 3c presents the coupling ratio from the input to the out-

put port (referred to an individual waveguide) of the devices. The nonadiabatic-pumping structure possesses a 1 dB bandwidth in the whole measured range from 1330 to 1650 nm, indicating a practical operation bandwidth of at least  $\approx 320$  nm ( $>400$  nm in simulation), which exhibits  $\approx 2$  times of the conventional DC ( $\approx 160$  nm) and extends to all of the optical communication bands (O-, E-, S-, C-, L-, and U-bands). In addition, Figure 3d shows that the device exhibits a general insertion loss (compared to an individual LN waveguide) less than 1 dB and a low crosstalk less than  $\approx 10$  dB, indicating a high performance of the designed light coupling structure via nonadiabatic pumping.

Furthermore, we also designed and fabricated various nonadiabatic-pumping-based structures to investigate the fabrication tolerance and robustness against structural deviations. Numerical and experimental results show that  $\approx 100$  nm variation of waveguide width/separation and  $\pm 10^\circ$  variation of the side wall angle can have slight influence on the performance of the ultrabroadband response, due to decreased dispersion of the accumulated phase contrast ( $\Delta\varphi$ ) in the nonadiabatic transition process (see Section S3 in the Supporting Information). Though the samples are fabricated based on the thin-film LN platform, we also demonstrate the ultrabroadband coupling based on nonadiabatic pumping with silicon-on-insulator (SOI) waveguides through numerical simulations (see Section S4 in the Supporting Information). Therefore, we can conclude

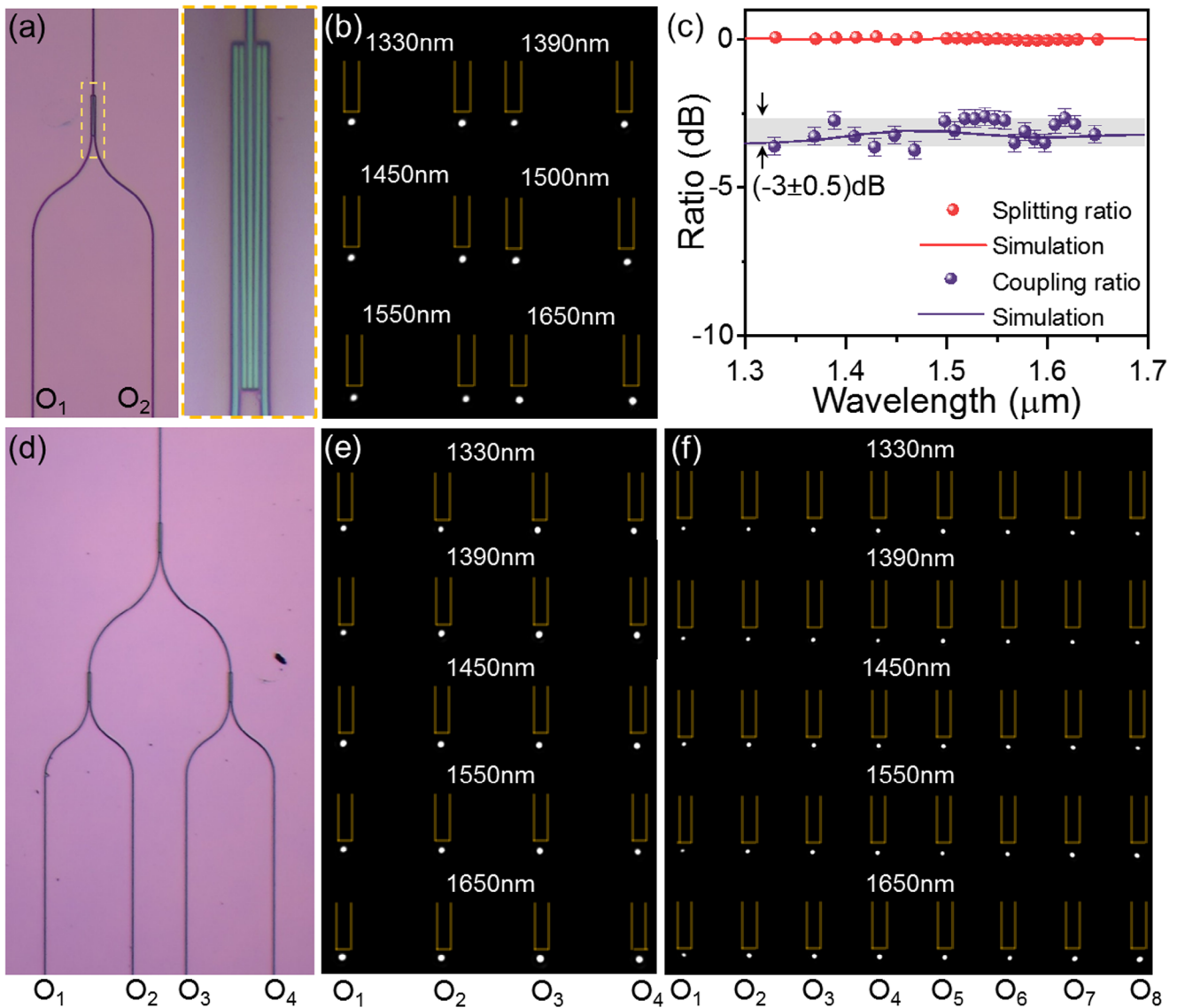


**Figure 4.** Broadband light routings based on nonadiabatic pumping design. a) Microscopic image of a 3 dB beamsplitter fabricated based on the nonadiabatic pumping coupler. b) Experimentally imaged scattering fields from output ports of the beamsplitter at different wavelengths (1330, 1390, 1450, 1500, 1550, and 1650 nm). c) Plots of measured and simulated coupling ratios and splitting ratios for the beamsplitter. d) Microscopic image of a two-level (4-port) cascaded networks. Experimentally imaged scattering fields from output ports of e) the two-level (4-port) and f) three-level (8-port) cascaded networks at different wavelengths (1330, 1390, 1450, 1550, and 1650 nm), respectively.

that the basic principle of nonadiabatic-pumping-induced dispersionless coupling is independent on materials. Figure 3e summarizes the experimentally measured performances of typical broadband coupling designs on chip (Table S1, Supporting Information).<sup>[10–13,15,30,37–40]</sup> The operation bandwidth of our nonadiabatic pumping device is 2–3 times broader than the other designs with similar interaction lengths. It should be noted that, although adiabatic passage transfer enables to provide a very broad coupling bandwidth, it requests a much longer interaction length on the order of millimeters,<sup>[10]</sup> which is about 20 times larger than the nonadiabatic pumping design. Therefore, our design preserves significant advantages simultaneously in extending the operation bandwidth and minimizing the footprint. The ultrabroadband operation bandwidth, great robustness,

and compatibility of this nonadiabatic pumping design show great potential for efficient light coupling and interconnection in versatile compact platforms.

### 3.3. Ultrabroadband Multiple-Level Cascaded Networks for Integrated Photonics

In order to demonstrate the promise of the ultrabroadband light coupling on chip, the nonadiabatic pumping structures are constructed to form complex functional devices for light routing. Figure 4a presents a microscopic image of a 3 dB beamsplitter produced by symmetrically aligning the nonadiabatic-pumping-based coupling elements. The enlarged part on right panel of

Figure 4a shows a uniform distribution of the two sides. As a consequence, the input signal can be equally split into two routes at different wavelengths, as shown in Figure 4b. Correspondingly, Figure 4c presents quantitatively simulated and measured coupling ratio and splitting ratio of the beamsplitter. The coupling ratio distributes in a range of  $(-3 \pm 0.5)$  dB, and the splitting ratio of the two ports ( $I_{O1}/I_{O2}$ ) remains nearly to be 1:1, for the whole measured wavelengths from 1330 to 1650 nm. It means that the broadband performance can still maintain for combined functional elements. Furthermore, the splitter elements are connected to form multiple-level cascaded networks, including two-level (4-port, Figure 4d,e) and three-level (8-port, Figure 4f) configurations. In the cascaded networks, the input light can be equally routed to all of the output ports with a same broadband response. It demonstrates that our broadband coupling strategy via nonadiabatic pumping is not only effective for individual element, but also powerful for constructing cascaded networks, showing great prospects for large-scale and compact photonic integration on chip.

## 4. Conclusion

An ultrabroadband light coupling strategy for on-chip integration has been developed via nonadiabatic pumping. The proposal has been successfully demonstrated in practice in a typical thin-film LNOI platform, which enables to realize ultrabroadband and efficient light coupling spanning from 1330 to 1650 nm (1 dB operation bandwidth of  $\approx 320$  nm), as well as with a small interaction length ( $50 \mu\text{m}$ )  $\approx 1/10$  of the adiabatic transfer regime. Moreover, the device exhibits a high performance with a low insertion loss ( $< 1$  dB), a low crosstalk ( $< -10$  dB), and a great robustness against structural deviations ( $\approx 100$  nm). For functional applications, this light coupling strategy is of remarkable convenience for constructing broadband beamsplitter and multiple-level cascaded networks for compact light routings and interconnects on chip. More importantly, it has been demonstrated that the basic principle is independent on materials and can be realized on versatile compact platforms. The nonadiabatic pumping designs preserve significant advantages in extending the operation bandwidth of light coupling and interconnection to all of the optical communication bands (O-, E-, S-, C-, L-, and U-bands), which shows great potential for realizing large-scale photonic integration, parallel WDM transmission, and high-speed information processing on chip.

## Supporting Information

Supporting Information is available from the Wiley Online Library or from the author.

## Acknowledgements

W.L. and C.L. contributed equally to this work. This work was financially supported by the National Natural Science Foundation of China (Grant Nos. 62375097, 12374305, 12204363, 12021004), the Natural Science Foundation of Hubei Province (Grant Nos. 2023AFB822, 2020CFA004), and the Hubei Key Laboratory of Optical Information and Pattern Recognition, Wuhan Institute of Technology (Grant No. 202202). The authors gratefully acknowledged the Center of Micro-Fabrication and Characterization (CMFC) of Wuhan National Laboratory for Optoelectronics (WNLO) (HUST) for their support in the nanofabrication of devices.

## Conflict of Interest

The authors declare no conflict of interest.

## Data Availability Statement

The data that support the findings of this study are available from the corresponding author upon reasonable request.

## Keywords

functional devices, integrated photonics, nonadiabatic pumping, ultra-broadband light coupling

Received: September 11, 2024

Revised: November 4, 2024

Published online: December 5, 2024

- [1] W. Bogaerts, D. Pérez, J. Capmany, D. A. B. Miller, J. Poon, D. Englund, F. Morichetti, A. Melloni, *Nature* **2020**, *586*, 207.
- [2] A. Rizzo, A. Novick, V. Gopal, B. Y. Kim, X. Ji, S. Daudlin, Y. Okawachi, Q. Cheng, M. Lipson, A. L. Gaeta, K. Bergman, *Nat. Photonics* **2023**, *17*, 781.
- [3] Y. Shen, N. C. Harris, S. Skirlo, M. Prabhu, T. Baehr-Jones, M. Hochberg, X. Sun, S. Zhao, H. Larochelle, D. Englund, M. Soljačić, *Nat. Photonics* **2017**, *11*, 441.
- [4] H. Feng, T. Ge, X. Guo, B. Wang, Y. Zhang, Z. Chen, S. Zhu, K. Zhang, W. Sun, C. Huang, Y. Yuan, C. Wang, *Nature* **2024**, *627*, 80.
- [5] Z. C. Du, K. Liao, T. X. Dai, Y. F. Wang, J. Z. Gao, H. Q. Huang, H. X. Qi, Y. D. Li, X. X. Wang, X. R. Su, X. Y. Wang, Y. Yang, C. C. Lu, X. Y. Hu, Q. H. Gong, *Sci. Adv.* **2024**, *10*, eadm7569.
- [6] J. Wang, F. Sciarino, A. Laing, M. G. Thompson, *Nat. Photonics* **2020**, *14*, 273.
- [7] P. I. Sund, E. Lomonte, S. Paesani, Y. Wang, J. Carolan, N. Bart, A. D. Wieck, A. Ludwig, L. Midolo, W. H. P. Pernice, P. Lodahl, F. Lenzini, *Sci. Adv.* **2023**, *9*, eadg7268.
- [8] Y. Liu, H. Zhang, J. Liu, L. Lu, J. Du, Y. Li, Z. He, J. Chen, L. Zhou, A. W. Poon, *Nat. Commun.* **2024**, *15*, 3645.
- [9] S. Longhi, *Phys. Rev. E* **2006**, *73*, 026607.
- [10] Y.-X. Lin, M. Younesi, H.-P. Chung, H.-K. Chiu, R. Geiss, Q.-H. Tseng, F. Setzpfandt, T. Pertsch, Y.-H. Chen, *Opt. Express* **2021**, *29*, 27362.
- [11] G. F. R. Chen, J. R. Ong, T. Y. L. Ang, S. T. Lim, C. E. Png, D. T. H. Tan, *Sci. Rep.* **2017**, *7*, 7246.
- [12] Y. Wang, Z. Lu, M. Ma, H. Yun, F. Zhang, N. A. F. Jaeger, L. Chrostowski, *IEEE Photonics J.* **2016**, *8*, 7101408.
- [13] W. Song, W. Sun, C. Chen, Q. Song, S. Xiao, S. Zhu, T. Li, *Laser Photonics Rev.* **2020**, *14*, 1900193.
- [14] N. V. Vitanov, A. A. Rangelov, B. W. Shore, K. Bergmann, *Rev. Mod. Phys.* **2017**, *89*, 015006.
- [15] W. Song, T. Li, S. Wu, Z. Wang, C. Chen, Y. Chen, C. Huang, K. Qiu, S. Zhu, Y. Zou, T. Li, *Phys. Rev. Lett.* **2022**, *129*, 053901.
- [16] R. Citro, M. Aidelsburger, *Nat. Rev. Phys.* **2023**, *5*, 87.
- [17] M. Switkes, C. M. Marcus, K. Campman, A. C. Gossard, *Science* **1995**, *283*, 1999.
- [18] M. Lohse, C. Schweizer, O. Zilberberg, M. Aidelsburger, I. Bloch, *Nat. Phys.* **2016**, *12*, 350.
- [19] S. Nakajima, T. Tomita, S. Taie, T. Ichinose, H. Ozawa, L. Wang, M. Troyer, Y. Takahashi, *Nat. Phys.* **2016**, *12*, 296.
- [20] Y. E. Kraus, Y. Lahini, Z. Ringel, M. Verbin, O. Zilberberg, *Phys. Rev. Lett.* **2012**, *109*, 106402.
- [21] M. A. Bandres, M. C. Rechtsman, M. Segev, *Phys. Rev. X* **2016**, *6*, 011016.

- [22] Z.-G. Chen, W. Tang, R.-Y. Zhang, Z. Chen, G. Ma, *Phys. Rev. Lett.* **2021**, 126, 054301.
- [23] W. Kao, K. Y. Li, K. Y. Lin, S. Gopalakrishnan, B. L. Lev, *Science* **2021**, 371, 296.
- [24] M. Lohse, C. Schweizer, H. M. Price, O. Zilberberg, I. Bloch, *Nature* **2018**, 553, 55.
- [25] S. K. Sridhar, S. Ghosh, D. Srinivasan, A. R. Miller, A. Dutt, *Nat. Phys.* **2024**, 20, 843.
- [26] Y. G. Ke, X. Z. Qin, F. Mei, H. H. Zhong, Y. S. Kivshar, C. Lee, *Laser Photonics Rev.* **2016**, 10, 995.
- [27] O. Zilberberg, S. Huang, J. Guglielmon, M. H. Wang, K. P. Chen, Y. E. Kraus, M. C. Rechtsman, *Nature* **2018**, 553, 59.
- [28] A. Cerjan, M. Wang, S. Huang, K. V. P. Chen, M. C. Rechtsman, *Light: Sci. Appl.* **2020**, 9, 178.
- [29] Y. K. Sun, X. L. Zhang, F. Yu, Z. N. Tian, Q. D. Chen, H. B. Sun, *Nat. Phys.* **2022**, 18, 1080.
- [30] L. Sun, H. Wang, Y. He, Y. Zhang, G. Tang, X. He, J. Dong, Y. Su, *Laser Photonics Rev.* **2022**, 16, 2200354.
- [31] F. Mei, G. Chen, L. Tian, S. L. Zhu, S. T. Jia, *Phys. Rev. A* **2018**, 98, 012331.
- [32] Z. Fedorova, H. X. Qiu, S. Linden, J. Kroha, *Nat. Commun.* **2020**, 11, 3758.
- [33] P. Titum, E. Berg, M. S. Rudner, G. Refael, N. H. Lindner, *Phys. Rev. X* **2016**, 6, 021013.
- [34] L. Privitera, A. Russomanno, R. Citro, G. E. Santoro, *Phys. Rev. Lett.* **2018**, 120, 106601.
- [35] S. Longhi, *Phys. Rev. B* **2019**, 99, 155150.
- [36] A. Boes, L. Chang, C. Langrock, M. Yu, M. Zhang, Q. Lin, M. Lončar, M. Fejer, J. Bowers, A. Mitchell, *Science* **2023**, 379, eabj4396.
- [37] H. Sattari, A. Y. Takabayashi, Y. Zhang, P. Verheyen, W. Bogaerts, N. Quack, *Opt. Lett.* **2020**, 45, 2997.
- [38] Z. Lu, H. Yun, Y. Wang, Z. Chen, F. Zhang, N. A. F. Jaeger, L. Chrostowski, *Opt. Express* **2015**, 23, 3795.
- [39] D. Guo, T. Chu, *Opt. Lett.* **2018**, 43, 4795.
- [40] L. Yu, J. Guo, H. Xiang, C. Liu, Y. Zhao, D. Dai, *J. Lightwave Technol.* **2024**, 42, 740.